SCIENTIFIC REP{O}RTS

OPEN

On the detection of cerebral metabolic depression in experimental traumatic brain injury using Chemical Exchange Saturation Transfer (CEST)-weighted MRI

Tsang-Wei Tu[1,2,3], Wael G. Ibrahim[4], Neekita Jikaria[1,2,5], Jeeva P. Munasinghe[6], Jaclyn A. Witko[1,2], Dima A. Hammoud[4] & Joseph A. Frank[1,7]

Metabolic abnormalities are commonly observed in traumatic brain injury (TBI) patients exhibiting long-term neurological deficits. This study investigated the feasibility and reproducibility of using chemical exchange saturation transfer (CEST) MRI to detect cerebral metabolic depression in experimental TBI. Phantom and *in vivo* CEST experiments were conducted at 9.4 Tesla to optimize the selective saturation for enhancing the endogenous contrast-weighting of the proton exchanges over the range of glucose proton chemical shifts (glucoCEST) in the resting rat brain. The optimized glucoCEST-weighted imaging was performed on a closed-head model of diffuse TBI in rats with 2-deoxy-D-[^{14}C]-glucose (2DG) autoradiography validation. The results demonstrated that saturation duration of 1–2 seconds at pulse powers 1.5–2μT resulted in an improved contrast-to-noise ratio between the gray and white matter comparable to 2DG autoradiographs. The intrasubject (n = 4) and intersubject (n = 3) coefficient of variations for repeated glucoCEST acquisitions (n = 4) ranged between 8–16%. Optimization for the TBI study revealed that glucoCEST-weighted images with 1.5μT power and 1 s saturation duration revealed the greatest changes in contrast before and after TBI, and positively correlated with 2DG autoradiograph ($r = 0.78$, $p < 0.01$, n = 6) observations. These results demonstrate that glucoCEST-weighted imaging may be useful in detecting metabolic abnormalities following TBI.

Cerebral metabolic abnormalities can be detected from weeks to years after injury[1–3] as reported for many traumatic brain injury (TBI) patients[4–6] as well as in animal studies[7–9]. Energy mismatch initiates neuro-metabolic cascades that could alter long-term cognition and hinder neurologic functions[2,6,10]. Prolonged decreases in metabolism may impair learning and memory[11–13], cause progressive cerebral atrophy[14] and place TBI patients at high risk for development of neurodegenerative diseases, such as dementia[15,16] and Alzheimer's disease[17,18]. Alterations in the cerebral glucose uptake and metabolism in TBI patients can be detected by 2 deoxy-2-(^{18}F) fluoro-D-glucose (^{18}F-FDG) positron emission tomography (PET) using ^{18}F as a pharmaceutical tracer[19]. PET scans are limited by low resolution and the inability to perform longitudinal studies due to ionizing radiation

[1]Frank Laboratory, Radiology & Imaging Sciences, Clinical Center, National Institutes of Health, Bethesda, MD, United States. [2]Center for Neuroscience and Regenerative Medicine, Henry Jackson Foundation, Bethesda, MD, United States. [3]Molecular Imaging Laboratory, Department of Radiology, Howard University, Washington, DC, United States. [4]Center for Infectious Disease Imaging, Radiology & Imaging Sciences, Clinical Center, National Institutes of Health, Bethesda, MD, United States. [5]Acute Stroke Research Section, National Institute of Neurological Disorders and Stroke, National Institutes of Health, Bethesda, MD, United States. [6]Mouse Imaging Facility, National Institute of Neurological Disorders and Stroke, National Institutes of Health, Bethesda, MD, United States. [7]National Institute of Biomedical Imaging and Bioengineering, National Institutes of Health, Bethesda, MD, United States. Correspondence and requests for materials should be addressed to T.-W.T. (email: tut@howard.edu)
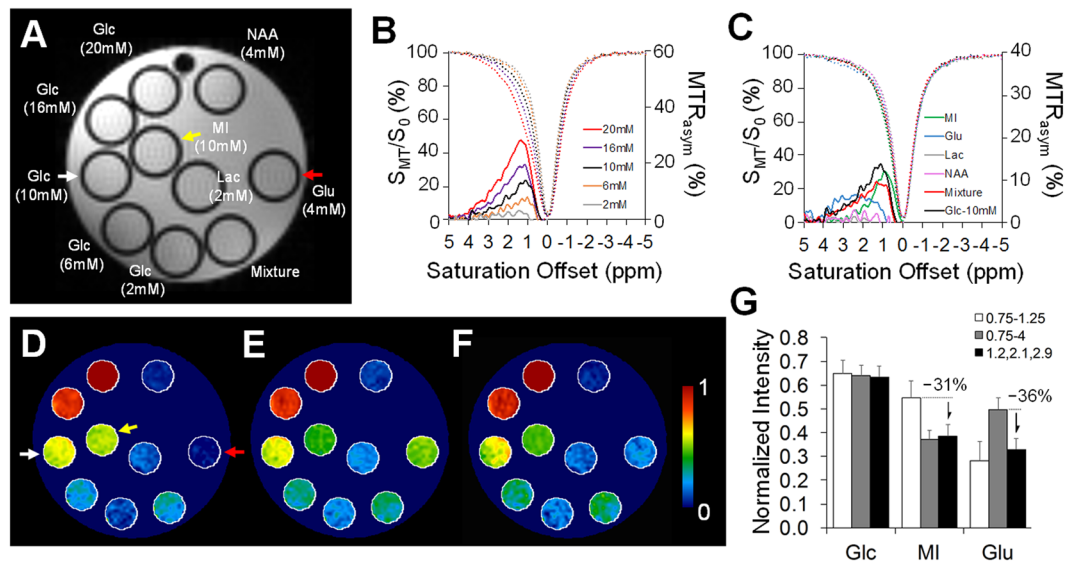
Figure 1. The CEST experiments on phantom metabolites consist of glucose (Glc, 2 to 20 mM), N-Acetylaspartic acid (NAA, 4 mM), myo-inositol (MI, 10 mM), lactate (Lac, 2 mM), glutamate (Glu, 4 mM) and a mixture of all metabolites (**A**). The Z-spectra and MTR$_{asym}$ curves are displayed for glucose (**B**) and other metabolites (**C**). Comparisons between the derivations of the glucoCEST-weighted imaging were obtained from integrating the MTR$_{asym}$ between 0.75–1.25 ppm (**D**) and 0.75–4.0 ppm (**E**) and 1.2 ($\pm$0.4), 2.1 ($\pm$0.2), 2.9 ($\pm$0.1) ppm (**F**). The quantification of Glc, MI, and Glu (arrows in **D**) shows that the current glucoCEST-weighted imaging improves the image contrast for glucose, while reducing ~30% contrast in MI and Glu. The representative glucoCEST-weighted images were acquired with a saturation power 5 uT and duration 2 s. The image intensity was normalized to its Glc (20 mM) intensity for comparison.

exposure limits. Moreover, analysis of PET scans requires the incorporation of a lumped-constant that is dependent on arterial plasma glucose concentration. However, variations in glucose levels across the normoglycemic range over repeated measurements in TBI patients tend to obscure results[20–22].

Recently, chemical exchange saturation transfer (CEST) magnetic resonance imaging (MRI) has been introduced as a sensitive, non-invasive technique with high spatial resolution that can detect various molecular species (e.g. glucose) via [1]H–water ^{1}H exchange without the need of radio-isotopes[23,24]. Multiple molecules, possessing exchangeable protons, can be evaluated at their respective chemical shifts by applying magnetization transfer (MT) saturation pulses over a range of frequency offsets across the water proton resonance frequency used as a reference (i.e. Z-spectrum)[25,26]. CEST MRI has been employed to evaluate glucose content, defined as glucoCEST. Contrast is generated by determining the asymmetry of MT ratio (MTR$_{asym}$) on the Z-spectrum in a range of glucose chemical shifts upfield and downfield of the water proton resonant frequency[27]. GlucoCEST imaging following an intravenous (IV) bolus of glucose as contrast agent has been used to successfully distinguish colorectal tumor types in rats[28] and characterize the perfusion-related properties and blood-brain barrier permeability in glioblastoma patients[29]. To date, the glucoCEST technique has not yet been utilized to explore changes of endogenous contrast within the resting brain.

The current study investigated the feasibility of using the glucoCEST-weighted imaging for detecting metabolic depression in the resting brain following TBI. A series of phantom experiments were performed to optimize the glucoCEST-weighted imaging parameters for glucose chemical shifts of 1.2, 2.1 and 2.9 part per million (ppm)[27,28,30]. Following the optimization of the CEST imaging parameters, we investigated the sensitivity and specificity of the image-contrast for assessing glucose concentrations. The glucoCEST-weighted imaging parameters were further evaluated in normal rat brains to determine the reproducibility and reliability of this approach over time. GlucoCEST-weighted imaging was then performed in a closed-head model of diffuse TBI in rats[31]. Results were compared to postmortem 2-deoxy-D-[^{14}C]-glucose (2DG) autoradiography to determine changes of glucose uptake and metabolism before and after TBI. With appropriate optimization of the MT parameters, the glucoCEST-weighted imaging technique was reproducible and has the potential to detect cerebral metabolic abnormalities during *in vivo* studies.

Results

Phantom study. The phantom experimental results are shown in Fig. 1. The Z-spectra and MTR$_{asym}$ curves obtained from the regions of interest (ROIs) in glucose (Glc) phantoms demonstrated the CEST effects from the Glc hydroxyl groups. Glc peaks were observable around 1.2, 2.1 and 2.9 ppm in the range of known biological concentrations (2–20 mM) (Fig. 1B). The Glc proton–water proton exchanges at the three resonances, however, were not clearly depicted because of the accelerated rate of exchanges between these pools of protons in the physiological pH level at 7.4[27]. Nevertheless, the MTR$_{asym}$ curves were clearly distinguishable between different Glc levels of the range in biological concentrations (Fig. 1B). The other metabolites in the phantom had different
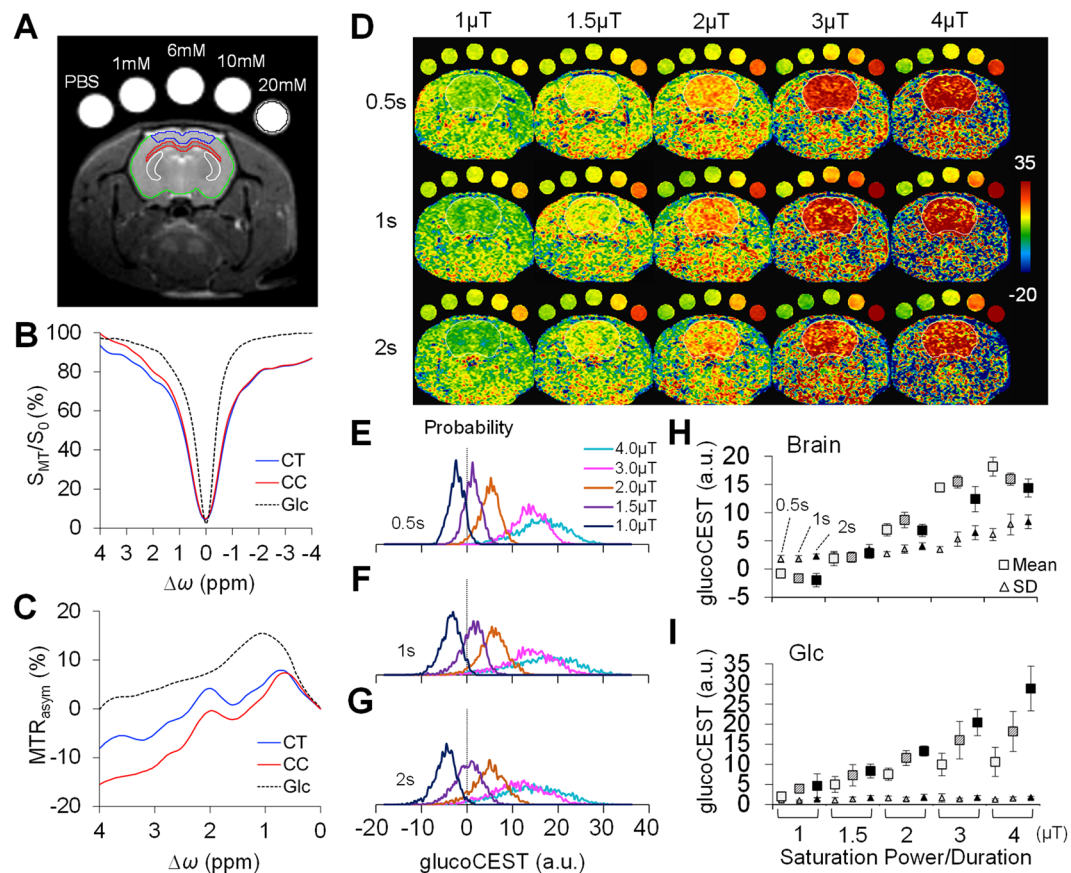
Figure 2. The setup for *in vivo* glucoCEST-weighted imaging on normal brains. Animals were imaged with five glucose phantoms consisting of 1 × phosphate-buffered saline (PBS), 1, 6, 10, 20 mM glucose (Glc) for comparison (**A**). The regions of interest denote the areas for data quantification of the cortex (CT, blue), corpus callosum (CC, red), caudate-putamen complex (Cpu, white, data used in Fig. 6), entire brain (green) and 20 mM glucose phantom (black). The Z-spectra (**B**) and the MTR$_{asym}$ curves (**C**) acquired by 2 μT and 1 s saturation pulses showed CEST signals of Glc, CT and CC. The representative glucoCEST-weighted images were acquired using various saturation power and duration (**D**). While the glucoCEST-weighted images show clear contrast in response to different concentrations in phantoms, the glucoCEST images also differentiate contrast between CT and CC in the brain. The probability density of the brain glucoCEST signals is approximately Gaussian distributed for saturation duration of 0.5 s (**E**), 1 s (**F**) and 2 s (**G**). The averaged glucoCEST-weighted data in the brains (n = 6) show an increased mean and standard deviation (SD) by applying higher saturation power (**H**). In contrast, the signals in the 20 mM phantom increased in proportion to higher saturation power duration, while their SDs appear low across all experiments (**I**). (**H**) and (**I**) for each saturation power, points from the left to right denote the data acquired by 0.5 s (empty symbols), 1 s (pattern symbols), and 2 s (solid symbols) for saturation duration.

exchangeable proton resonance offsets including myo-inositol (MI) 0.1 to 1.2 ppm; glutamate (Glu) with a broad coverage from 0.8 to 4 ppm and a peak at 3 ppm; and lactate (Lac) and N-Acetylaspartic acid (NAA) with negligible signals when employing the current acquisition parameters (Fig. 1C). Compared to the glucoCEST by integrating MTR$_{asym}$ from 0.75–1.25 ppm[32] (Fig. 1D) and 0.75–4.0 ppm[28] (Fig. 1E), the glucoCEST-weighted image derived from 1.2 (±0.4), 2.1 (±0.2) and 2.9 (±0.1) ppm (Fig. 1F) resulted in an approximate 30% decrease in signal intensity for MI and Glu (Fig. 1G), while still being able to maintain relevant contrast corresponding to the various Glc concentrations. A linear relationship (r > 0.9, p < 0.01, n = 5) was observed between the glucoCEST-weighted image contrast and the Glc concentration when MT saturation power was ≥1 μT (see Supplementary Fig. S1).

Optimization of saturation amplitudes for *in vivo* brain imaging. Figure 2 shows the *in vivo* glucoCEST-weighted imaging data obtained from rat brains. The averaged Z-spectra for the brains (n = 6) differed from the Glc phantoms due to interactions from radiofrequency (RF) irradiation effects and the presence of multiple metabolites in both cerebral cortex (CT) and corpus callosum (CC) (Fig. 2B). The Glc peaks in the *in vivo* MTR$_{asym}$ profiles were not clearly apparent due to the effects of physiological pH level (~7.4) and overlapping exchangeable proton resonances from multiple metabolites in the brain (Fig. 2C). Figure 2D presents the series of *in vivo* glucoCEST-weighted images acquired from five Glc phantoms arranged in an array of saturation power and duration. Similar to the phantom data (Fig. 1 and Supplementary Fig. S2), the histograms of the brain glucoCEST appeared to have a Gaussian distribution (Fig. 2E–G). The kurtosis and skewness of

the glucoCEST-weighted signals in the brain were not different throughout all evaluated saturation amplitudes, although there was an increasing deviation in kurtosis at 4 μT. While negative values appeared in the brain glucoCEST-weighted images at the saturation power of 1 μT, the intrasubject mean signal increased in proportion to the saturation power from 1 to 3 μT (Fig. 2H). No significant increases in glucoCEST-weighted signals were detected with increasing saturation powers from 3 to 4 μT. At all saturation powers, the glucoCEST-weighted signals using 2 s saturation pulses showed lower values when compared to those of shorter duration pulse of 0.5 s and 1 s. The intrasubject standard deviation (SD) of the glucoCEST-weighted signals increased significantly ($p < 0.05$, n = 6) when applying saturation powers ≥ 3 μT to the brains. The SDs for the long saturation duration (2 s) also tended to increase as compared to the shorter duration (0.5 s) (Fig. 2H). In contrast, the signals in the 20 mM Glc phantom were consistently increased in proportional to both the saturation power and duration. However, the measured within-phantom SDs for all the tested saturation amplitudes were consistently low (Fig. 2I).

The group-averaged glucoCEST-weighted signals between subjects increased with the saturation power from 1 to 3 μT in the cortex (CT), while in the corpus callosum (CC) there was a significant ($p < 0.05$, n = 6) increase observed at saturation powers ≥ 1.5 μT (Fig. 3A–C). For both CT and CC, the glucoCEST-weighted signals leveled out above a saturation power of 3 μT and saturation duration of 1 and 2 s (Fig. 3B,C). The contrast-to-noise ratio (CNR) between CT and CC decreased in proportional to the increased saturation power and the decreased duration (Fig. 3D). In comparison, the CNRs in the Glc phantoms continued to increase with increasing saturation powers and durations (Fig. 3E).

Reproducibility of *in vivo* brain glucoCEST-weighted images.
The *in vivo* brain glucoCEST-weighted images were reproducible across multiple scans (Fig. 4). The intrasubject coefficient of variation (CoV) was 8.4 ± 2.2% for the brain and 2.2 ± 0.6% for the Glc phantom in 4 continuous CEST experiments acquired within 2.5 hours (Fig. 4A). In comparison, when *in vivo* brain glucoCEST-weighted images were acquired weekly over 28 days, there was a CoV of 15.1 ± 2.9% for the brain and 7.2 ± 2.4% for the Glc phantom (Fig. 4B). The intersubject CoV was 16.4 ± 5.5% between animals and 7.8 ± 6.3% for the Glc phantoms. The averaged glucoCEST-weighted images showed significant differences (p < 0.01, n = 3) in values obtained from the CT (4.0 ± 0.3 a.u.) compared to the CC (−1.3 ± 0.2 a.u.) and 20 mM Glc phantom (8.3 ± 0.4 a.u.) (Fig. 4C,D).

TBI study.
TBI experiments were performed using a modified Marmarou weight drop closed-head injury model[31]. The 2DG autoradiographs displayed significant ($p < 0.01$, n = 3) difference in 2DG uptake in the CT (295.2 ± 43.8 nCi/g) and CC (129.2 ± 16.8 nCi/g) of the normal rats (Fig. 5A), with the intersubject CoV of 10.7%. Two weeks following TBI, autoradiographs clearly demonstrated decreases in 2DG uptake in the CT (186.0 ± 14.4 nCi/g) and CC (84.0 ± 10.6 nCi/g) (Fig. 5B,C). A wide variation in 2DG uptake was observed with significant ($p < 0.01$, n = 3) changes in the CC, CT, caudate-putamen complex (CPu) and thalamus in the injured brains. The glucoCEST-weighted images obtained with 1.5 μT and <2 sec saturation pulses showed a clear pattern of decreasing contrast within the brains that was consistent with the 2DG observations (Fig. 5A,B). In comparison, the glucoCEST-weighted images performed at 3 μT demonstrated stronger RF irradiation effects especially in the ventral and lateral side of the brain at locations of greater field inhomogeneities. Histogram analysis of the glucoCEST-weighted images revealed that following TBI, the images exhibited significant decreases (t = 99.7, $p < 0.01$, n = 12) on the image obtained with a saturation power of 1.5 μT and 1 s duration (Fig. 5C). Further analysis revealed that by acquiring glucoCEST-weighted images with saturation power of 3 μT and 1 s duration, image contrast changes were reduced between the normal and TBI brains, yet the image contrast was still significantly different (t = 3.4, $p < 0.05$, n = 12).

The correlation analysis revealed a moderate correlation ($r = 0.52$–0.78, $p < 0.01$, n = 6) between the changes in autoradiographs and the glucoCEST-weighted images quantified from the external capsule, CC, CT and Cpu. (Fig. 6A–D). The corresponding Bland-Altman analysis showed that the glucoCEST-weighted images of 1.5 μT saturation power and 1 s duration were in an agreement with a higher correlation level ($r = 0.78$, $p < 0.01$, n = 6) to 2DG autoradiographs (Fig. 6E,F). The 3 μT group exhibited a greater bias on the mean difference to the autoradiographic results (Fig. 6G,H).

Discussion
The primary injury in diffuse TBI results initially in widespread parenchymal damage followed by secondary pathological processes. These include various physiological deficiencies, such as hypoxia, decreased blood flow, hyperglycemia and abnormal cerebral metabolism, which are associated with poor neurological outcome[6,33–35]. Invasive brain microdialysis techniques are widely used in monitoring brain glucose to detect the early signs of secondary injuries[36–38]. The crux of TBI patient care centers on the maintenance of adequate cerebral blood flow (CBF) in order to preserve tissues from irreparable damage caused by insufficient delivery of oxygen and glucose[20,39,40]. Likewise, insulin therapies have been evaluated in TBI patients as a method to regulate blood glucose in order to prevent further deterioration of brain tissue[41–43]. Thus, there is an increasing demand for a non-invasive imaging technique capable of evaluating glucose metabolism to inform the clinical and rehabilitative management of TBI patients[44,45].

The current study describes a "proof-of-concept" investigation on the development, optimization and validation of glucoCEST-weighted imaging in a rat model of diffuse TBI. Following TBI, the glucose levels in the CT and CC were decreased by 46.9 ± 15.9% and 56.5 ± 13.6%, respectively, on 2DG autoradiographs, suggesting a hypometabolic state (Fig. 5). This hypometabolic phase in TBI is thought to be the consequence of a systematic decrease in CBF[46], defects in glucose transporter function[13,47], loss of neuronal integrity[48] or decreased demand for glucose in tissues[10,49]. We observed comparable contrast changes with glucoCEST-weighted images following TBI (Fig. 5).
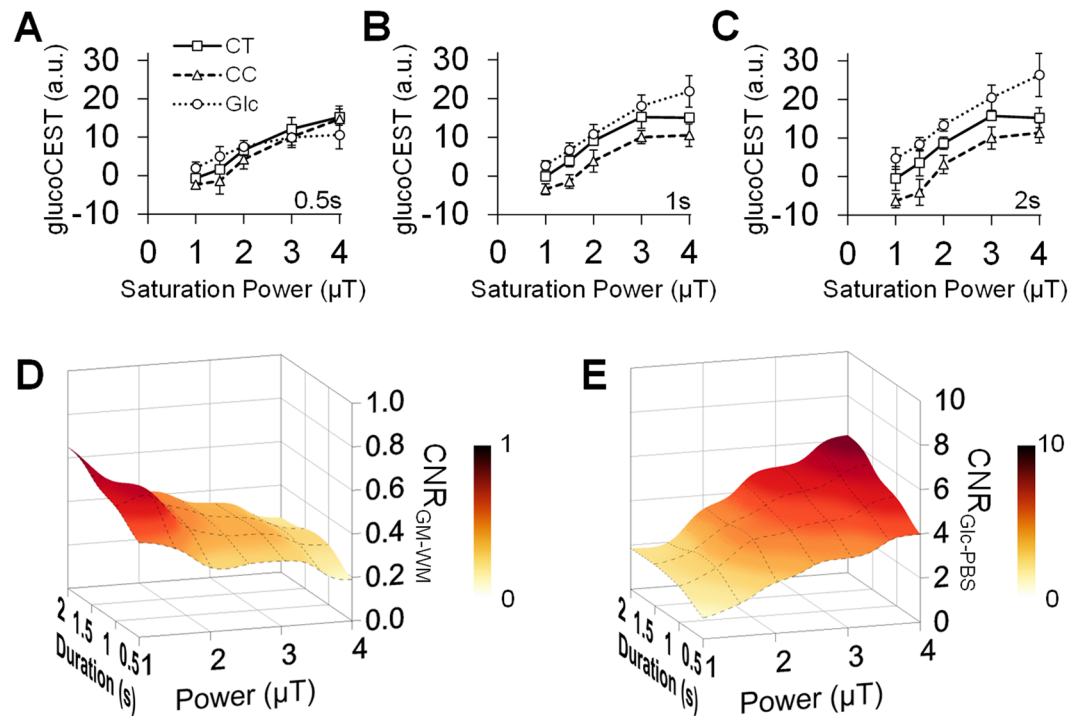
Figure 3. Comparison of the glucoCEST-weighted image contrast in brain and glucose phantom in response to multiple saturation amplitudes by saturation duration 0.5 s (**A**), 1 s (**B**) and 2 s (**C**). The resulting contrast-to-noise ratio (CNR) between the gray-white matter is maximized when applying saturation power $\leq 2\mu T$ and saturation duration 1–2 s (**D**). The CNRs in the Glc phantom increase with higher saturation power and longer saturation duration (**E**). CT: cortex, CC, corpus callosum, Glc: glucose, PBS: phosphate-buffered saline.
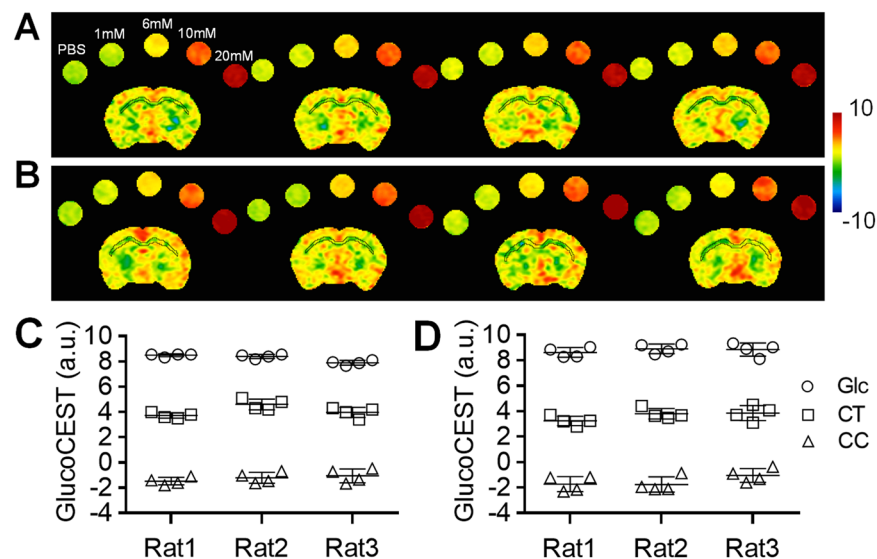

Figure 4. Representative glucoCEST-weighted images of repeating scans display consistent contrast in the brain from four continuous scans (**A**) and four weekly scans (**B**). The ROI quantification of the cortex shows an intrasubject coefficient of variation $8.4 \pm 2.2\%$ in the continuous scans (**C**) and $15.1 \pm 2.9\%$ in the weekly scans (**D**) (n = 3). CT: cortex, CC, corpus callosum, Glc: glucose, PBS: phosphate-buffered saline.

A recent study performed in head and neck cancer patients reported that glucoCEST-weighted imaging was able to differentiate between endogenous glucose content within the tumor and surrounding normal tissue[50]. Following an intravenous injection of glucose, it was shown that increased levels of glucose in the circulation enhanced the contrast differences between pre- and post-contrast glucoCEST-images within tissues. However, the
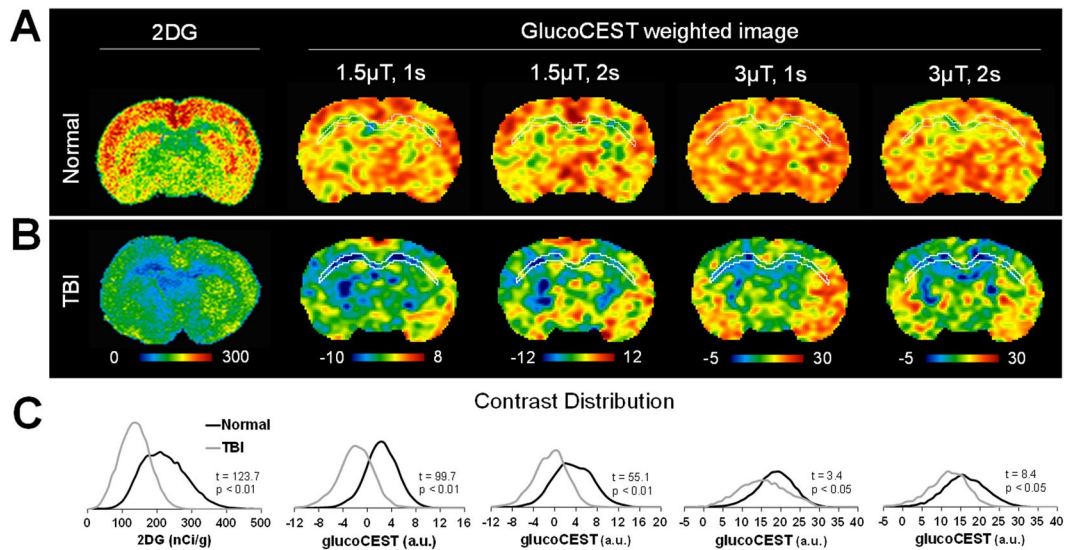
Figure 5. Comparison of the 2DG autoradiographs and glucoCEST-weighted images in the normal (**A**) and TBI brains (**B**). The images are scaled to mean $\pm 3 \times$ standard deviation of the contrast in each group for cross comparison. The histograms of autoradiographs and glucoCEST-weighted images show the relative contrast shift between the normal and TBI brains (**C**).

high concentration of intravenous glucose needed to obtain such increases in image contrast may be detrimental to brain physiology by introducing alterations in CBF, osmotic pressure and membrane transport[50]. Meanwhile, glucoCEST contrast using saturation pulses of $1 \mu T$ and $5 s$ at $7 T$ have been effective in detecting glucose and glycogen in the kidney during the progression of diabetic nephropathy[51]. The current study demonstrates that glucoCEST-weighted images at $9.4 T$ could be optimized for endogenous contrast within brain with limited variability in repeated measures (Fig. 4). Acquiring glucoCEST-weighted images at high magnetic fields allows prolonged storage of saturation in the water pool, enhances the saturation efficiency and the frequency separation of hydroxyl protons by better adherence to the slow-exchange condition and reduces interference from direct water saturation[52–57]. Combined, these factors result in improved image contrast at high magnetic fields.

Optimizing image acquisition for *in vivo* CEST MRI was necessary in order to monitor ongoing pathological and physiological changes in normal and disease conditions. In the CEST Z-spectrum, the glucose hydroxyl groups resonate around 1.2, 2.1 and 2.9 ppm downfield from water with fast exchange rates of 500–1500 s^{-1} [27,28,30]. According to two-site exchange theory, these rapidly exchangeable protons can be saturated efficiently by applying high saturation power, however, extensive direct saturation (DS) effects can occur, decreasing sensitivity of glucoCEST in the brain[58]. The DS effect in combination with the solid pool macromolecular magnetization transfer contrast (MTC), and the intra/intermolecular nuclear overhauser enhancement (NOE) could also be amplified in the brain, thereby complicating the quantification of the CEST contrast at lower frequency separations from water[26,59]. Although the MTR$_{asym}$ analysis could partially filter out the symmetric component of the DS effect, the asymmetric MTC and NOE from aliphatic protons of macromolecules/metabolites still exist in the brain. These compete with glucose in the same chemical shift range of desired proton exchange. Therefore, more critical RF irradiation levels and validation studies will be required for *in vivo* brain glucoCEST-weighed imaging to detect metabolic abnormalities.

In the current study, the RF irradiation level for *in vivo* glucoCEST was optimized based on the comparison of results obtained with 2DG autoradiography in the rat brain (Figs 5 and 6). 2DG is a glucose molecule whose 2-hydroxyl group is replaced by hydrogen so that glycolysis cannot proceed after phosphorylation to 2-deoxy-D-glucose-6-phosphate (2DG6P) by hexokinase. It serves as a good marker for glucose uptake and hexokinase activity in brain parenchyma[60]. In our experiments, 2DG was injected 45 minutes prior to euthanasia in order to reach a steady-state between glucose supply and consumption within the brain. The level of glucose uptake was clearly distinguishable between gray and white matter by 2DG (Fig. 5). High levels of glucose uptake were observed in the CT and CPu on autoradiographs[60], whereas lower optical density was detected in the CC and ventral striatum (around half of that observed in CT and CPu[61,62]). This pattern was also seen in the glucoCEST-weighted images acquired with low saturation amplitude (Fig. 5A), although few discrepancies appeared in the ventral and lateral side of the brain that might be associated with greater B$_0$ field inhomogeneities.

The *in vivo* glucoCEST signals from the rat brain were approximately Gaussian distributed (Fig. 2E–H), suggesting that the sequence parameter set was sensitive to random proton exchange processes in the parenchyma. However, when applying saturation powers $> 3 \mu T$, the variance of the signal distributions increased, reducing the CNR between CT and CC due to the excessive DS effect on the water spillover to the surround proton resonances. Applying a saturation power $< 1 \mu T$ resulted in low-labeling efficiency of the hydroxyl protons which caused an attenuated CEST effect such that the MTC and NOE effects become dominant and generate a negative MTR$_{asym}$. In contrast to the prolonged saturation duration (4.8–6 s) in previous dynamic glucoCEST enhancement (DGE) studies[28,32], we observed that a saturation duration $\leq 2 s$ was needed for the glucoCEST-weighted imaging to
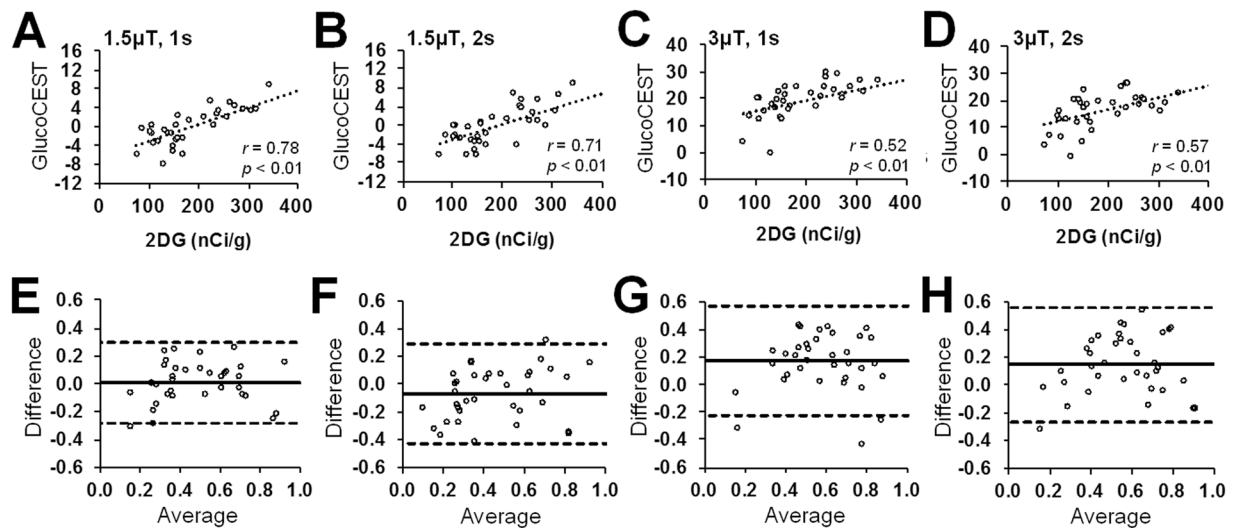
Figure 6. The correlations (**A**–**D**) and Bland-Altman plots (**E**–**H**) reveal the relationship and difference between the 2DG autoradiographs and the glucoCEST-weighted images acquired by different saturation pulses: 1.5 μT, 1 s (**A,E**), 1.5 μT, 2 s (**B,F**), 3 μT, 1 s (**C,G**) and 3 μT, 2 s (**D,H**). A higher correlation ($r = 0.78$, $p < 0.01$, n = 6) and agreement (95% CI: −0.28–0.30) are seen between the autoradiographs and glucoCEST-weighted images by 1.5 μT, 1 s saturation pulses, where the 3 μT, 1 s saturation presents a lower level of correlation ($r = 0.52$, $p < 0.01$, n = 6) and agreement (95% CI: −0.23–0.57) to the autoradiographs.

observe the contrast between gray and white matter at 9.4 T. In TBI brains, there was higher correlation observed between the 2DG and glucoCEST-weighted images acquired using low saturation power (1.5–2 μT) and short saturation duration (1–2 s), even in the presence of MTC and NOE effects (Fig. 6).

Validating the origin of the glucoCEST contrast is crucial for monitoring changes associated with pathology. A recent study investigated the source of the dynamic glucoCEST contrast by coupling the infusion of glucose and CBF measures by MRI along with NMR spectroscopy[32]. This study showed that the dynamic glucose-enhanced signals of glucoCEST in rat brains were not affected by cerebral or plasma pH nor correlated with hypercapnia-induced alterations of CBF. The glucoCEST signals were related to the intracellular concentration of glucose by comparing the dynamic contrast difference between the D- and L-glucose infusions since L-glucose does not enter cells. By correlating in vivo ³¹P NMR measurements of infused 2DG6P in the rat with glucoCEST signals, the study suggested that the glucoCEST signals could be related to glucose uptake and metabolism.

Endogenous glucoCEST contrast in the brain has not been well understood. Presumably, endogenous glucoCEST contrast is related to steady-state glucose and other intracellular metabolites that resonate between 0.75–2.9 ppm. However, the overlapping signals from multiple metabolites, such as MI, that resonate between 0.1–1.2 ppm confound the measurement of glucose on glucoCEST-weighted images. In the current study, the glucoCEST-weighted images were derived by focusing on the glucose proton exchanges and narrowing the integration of MTR$_{asym}$ at glucose chemical shifts, thereby reducing the interference from other metabolites (Fig. 1D–F). Following TBI, cerebral MI significantly increases as detected by ¹H-NMR spectroscopy studies[63–65] and has been attributed to increased astrogliosis[31,66], whereas glucose uptake is known to decrease[2,4,7,8]. In the current study, we were able to show that endogenous glucoCEST contrast was decreased following TBI and correlated to the findings on 2DG autoradiography. Further investigation is required to determine if the contribution of MI signal "subtracts" or "adds" contrast to glucoCEST-weighted imaging in TBI.

Limitations of this study need to be discussed to avoid misinterpretation of the results. First, the current study did not survey a complete neuro-metabolic profile in the TBI brains to determine the contribution from other metabolites (e.g. glutamate, NAA, lactate or MI) to glucoCEST contrast. The correlation between glucoCEST and 2DG autoradiography does not exclude the possibility that other metabolites might also contribute to changes in image contrast following TBI. Secondly, relating glucoCEST contrast to 2DG autoradiographs is not straightforward. In theory, the 2DG autoradiography measures the metabolic rate of glucose by acquiring the signal from the intracellular 2DG6P that is accumulated after 45 min of metabolism and washout. The endogenous glucoCEST signal, however, may represent total glucose from the sum of intra- and extra-cellular space, which requires further investigation. Meanwhile, the glucoCEST-weighted imaging was acquired on the rats under anesthesia, whereas the 2DG autoradiography was acquired in awake rats for a 45 min circulation time. Although imaging and 2DG results both observed metabolic abnormalities in TBI brains, the level of glucose metabolism might be underestimated by glucoCEST imaging[67]. In addition, there were significant partial volume effects when comparing 800 μm thick CEST images to 20 μm 2DG autoradiography sections. It is also important to note that the Glc peaks may not be apparent in several conditions, including high glucose concentration, pH > 6.2, or under multiple complications from other metabolites in the living tissue[27]. The addition of advanced acquisition or post-processing techniques, such as the multi-pool proton exchange model[68,69], Lorentzian decomposition of the CEST Z-spectra[70,71] or on-resonance spin-lock techniques[72,73] might provide mechanisms to better isolate glucose resonances from other metabolites.

Previous studies have reported high reproducibility (CoV < 3%) in repeated CEST experiments[74–76], but unfortunately the demonstration of reproducibility between laboratories of CEST MRI is difficult due to strong dependence on the saturation efficiency in each experimental setting[26]. The optimized parameters in the current study may not be applicable to other MR systems using different imaging parameters (e.g., volume, surface or phase array RF coils, etc.). Other factors including the temperature, proton exchange-rate in living tissue, pH level, T_1, T_2, the location of a subject within RF coil and RF pulse amplitude may also affect the contrast generated on CEST images[77]. Standardized procedures for optimization must be established for the CEST imaging parameters to ensure reproducible results[58]. Future studies should also include pathological, spectroscopic or molecular investigations to increase specificity for endogenous glucose detection in normal and injured brains, and examine how they compare to the observed glucoCEST-weighted images.

Methods

Phantom study.
Phantom experiments were conducted to characterize the Z-spectrum and MTR_{asym} of glucose by a Doty quadrature coil (Doty Scientific, Inc., Columbia, SC) in a Bruker 9.4 T scanner (Bruker Corp., Billerica, MA). The phantom consisted of five glucose concentrations mimicking *in vivo* brain levels (2–20 mM)[78], together with the other common brain metabolites in biological concentrations, including NAA (4 mM), MI (10 mM), Lac (2 mM), Glu (4 mM)[79] and a tube containing a mixture of these metabolites (Fig. 1A). The metabolite tubes were immersed in the $1 \times$ phosphate-buffered saline (PBS) and all the solutions were corrected to the physiological pH 7.4. The magnetic field (B_0) experienced within a volume of $30 \times 30 \times 5$ (mm^3) was made as homogenous as possible by 1st and 2nd order optimization of shimming (half height line width of <10 Hz). The CEST data were acquired by 2D Rapid Acquisition with Relaxation Enhancement (RARE) sequence with (S_{MT}) and without (S_{M0}) MT preparation pulses by repetition time (TR) 3.10 s, echo time (TE) 10.39 ms; RARE factor 4; number of excitation (NEX) 1; in plane resolution 400 μm^2, slice thickness 800 μm. The effect of MT pulse amplitudes on the sensitivity and specificity for glucose detection were inspected by arraying the saturation power from 0.5 to 10μT and saturation duration from 0.5 to 3 s. The Z-spectrum was acquired from the MT frequency offsets ($\Delta\omega$) from −2 to +2 kHz with 50 Hz frequency stepping, as a result, 81 points were sampled to delineate the Z-spectrum from −5 to +5 ppm.

Data processing for the glucoCEST-weighted image.
Procedure according to the WAter Saturation Shift Referencing (WASSR) method[80] was applied to correct the B_0 and B_1 field inhomogeneity of the CEST data. In brief, a separate WASSR dataset was acquired with small saturation amplitude (0.2μT for power and 0.1 s for duration) from −0.4 kHz to + 0.4 kHz with 10 Hz frequency stepping to obtain the B_0 field map. The CEST Z-spectrum was interpolated to 0.1 ppm stepping and fitted to Lorentzian line shapes in combination with WASSR data to correct the shifted water resonance frequency by B_0 field inhomogeneity. The B_1 field map was obtained by the same RARE sequence with two flip angle (30° and 60°) and the pixel-wise B_1 values were calculated by solving the equation [1]:

$$\frac{\cos 2\theta}{\cos\theta} = \frac{S(2\theta)}{S(\theta)}, \tag{1}$$

where $S(\theta)$ and $S(2\theta)$ are the pixel signals in an image with preparation flip angle θ and 2θ respectively. The B_1 field map was obtained by $B_1 = \theta(360\tau)^{-1}$. The coefficient B_1/B_{1ref} was used for B_1 correction of glucoCEST contrast, where B_{1ref} was the reference images for RF pulse amplitude of a 30° flip angle. After correction, the robust CEST parameter, the MTR_{asym} was derived by[74,79]:

$$MTR_{asym}(\Delta\omega) = \frac{S_{MT}(-\Delta\omega) - S_{MT}(\Delta\omega)}{S_{MT}(-\Delta\omega)}, \tag{2}$$

where $S_{MT}(-\Delta\omega)$ and $S_{MT}(\Delta\omega)$ are respectively the upfield and downfield MT signal intensity around the water resonance frequency at 0 Hz. The pixel-by-pixel signals of the glucoCEST-weighted image were generated by integrating the area under the MTR_{asym} curves at the glucose chemical shifts in 1.2 (±0.4), 2.1 (±0.2) and 2.9 (±0.1) ppm[28,30] with an arbitrary unit (a.u.). Results were compared to the previous derivation definition of glucoCEST using 0.75–1.25 ppm[32] and 0.75–4.0 ppm[28] for showing the effect of reducing interactions from other metabolites.

Rat model of diffuse TBI.
All animal studies were approved by the animal care and use committee at the National Institutes of Health, and experiments were performed according to the National Research Council's Guide for the Care and Use of Laboratory[81]. Female 8-week-old Sprague-Dawley rats (Taconic, Hudson, NY) were used in the TBI study. Rats first underwent baseline T2-weighted (T2W) images by RARE (TR 3.8 s, TE 15 ms, RARE factor 8, in-plane resolution 100 μm^2 with 500 μm slice thickness) according to a previously published screening guideline to exclude the complication of spontaneous ventriculomegaly or impaired circulation system that might affect the perfusion and glucose metabolism[82]. Eight rats were identified as having normal morphology and treated with a modified version of the Marmarou weight drop closed-head injury for diffuse TBI as previously described[31]. Another six rats with normal morphology were served as the control group and used for the reproducibility experiments.

In vivo MRI.
Imaging was conducted two weeks after TBI to evaluate the changes in cerebral glucose uptake between the normal controls and TBI animals. Animals were anesthetized using an isoflurane/oxygen mixture via nosecone. The isoflurane level was maintained minimum (0.7–1.5%) for the MRI, right above the level that the animals moved. The body temperature was maintained at 37 °C using a circulating water bath; a steady respiration rate (47 ± 3 bpm) was maintained by anesthesia control. Three-dimensional T$_2$*-weighted images were acquired

for examining the presence of hemorrhage by multiple gradient echo: TR 60 ms, TE 3.18 ms, echo spacing 3.25 ms, voxel size 200 μm³ (isotropic). 2 rats were found with hemorrhage and they were excluded in the subsequent TBI study to eliminate the complication of hemorrhage in deviating the local field homogeneity for an accurate MTR_{asym} estimation. Glass capillaries filled with $1 \times PBS$ and four concentrations of glucose solution (1, 6, 10 and 20 mM) were placed equidistantly above the rat head and imaged with the brain for comparison (Fig. 2A). 2nd order Mapshim was applied to cover the brain in a $16.5 \times 14.1 \times 6.5$ (mm) FOV to reach 40–50 Hz line widths for field homogeneity. The CEST data were acquired using the same imaging setting in the phantom experiment by RARE: TR 2.06 s, TE 10.39 ms; RARE factor 4; NEX 1; in plane resolution 354 μm², slice thickness 0.8 mm. An optimization study was conducted to determine the ideal combination of MT saturation power and duration for enhancing the detection of endogenous glucose in the rat brain. MT preparation pulses were arrayed for saturation power from 1, 1.5, 2, 3 and 4 μT, and saturation duration from 0.5, 1 and 2 s. The Z-spectrum was acquired from −1.6 to +1.6 kHz with 100 Hz frequency stepping to sample 33 points covering the frequency offset range from −4 to +4 ppm. The WASSR data for the rat brain were collected by the same RARE parameters with small saturation amplitude: power 0.3 μT, duration 0.25 s, frequency offset −0.4 to +0.4 kHz with 80 Hz frequency stepping. The *in vivo* Z-spectra were corrected for the B_0/B_1 field inhomogeneity to derive the MTR_{asym} curves and the glucoCEST-weighted images of the brains. The reproducibility of the *in vivo* brain glucoCEST was conducted on 3 normal rats by comparing 4 continuous acquisitions repeated in 2.5 hours, and 4 weekly acquisitions over 28 days with saturation power 1.5 μT, duration 1 s, and NEX 2.

2-deoxy-D-[¹⁴C]-glucose (2DG) autoradiography.

After MRI, three rats per group were randomly picked for 2DG autoradiography. Rats were anesthetized with isoflurane (3% with 700cc/min O_2) and $[^{14}C]-2DG$ (American Radiolabeled Chemicals Inc., St Louis, MO) was delivered as an intravenous bolus injection of 125μCi/kg body weight via the tail vein. Animals were awake for a tracer circulation time of 45 minutes, and then euthanized by isoflurane overdose, decapitated and brains were rapidly removed. The brains were then submerged shortly in 0.3 M sucrose on the ice, sectioned into 3 mm sections, frozen on dry ice and stored at −80 °C. Blocks were cut in a cryostat at −15 °C in 20 μm thick coronal sections then dried on glass slides. Slides were covered with scintillating sheets and exposed for 18 hours together with $[^{14}C]$ standard (ARC-146C(PL); St. Louis, MO) then analyzed in Microimager (Biospace lab, France). Measurements were performed on selected regions of interest (ROIs) placed in gray matter from CT and white matter in CC. Counts obtained from each slide were calibrated on the $[^{14}C]$ standard and values were then converted to nCi/g tissue.

Imaging and 2DG data analysis.

The Z-spectra, MTR_{asym}, and glucoCEST data were analyzed through ROIs on each metabolite tube for the phantom data (Fig. 1A), and on the entire brain, CT and CC of the brain sections matching to those on the autoradiographs (Fig. 2A). The characteristics of the glucoCEST contrast were analyzed for signal distributions examining skewness, kurtosis and variance under different saturation amplitudes. The CNR was derived by[83]:

$$CNR = \frac{glucoCEST_a - glucoCEST_b}{\sqrt{(\sigma_a^2 - \sigma_b^2)/2}} \cdot \frac{1}{\sqrt{TR \cdot NEX}},$$

(3)

where $glucoCEST_a$ and $glucoCEST_b$ are the mean intensity obtained from 20 mM glucose and PBS for the phantom data, and from CT and CC for the *in vivo* data; and σ_a and σ_b are their standard deviation (SD), respectively. For the TBI study, four glucoCEST data sets were acquired at two saturation powers (1.5 and 3 μT) and at two saturation durations (1 and 2 s). These glucoCEST-weighted images were compared to the autoradiographs for the sensitivity in detecting cerebral glucose changes following TBI. The autoradiographs were down-sampled to match the image resolution of the glucoCEST-weighted images. Each glucoCEST-weighted images and 2DG autoradiographs were normalized to its dynamic range (mean $\pm 3 \times SD$) of the image intensity in order to evaluate the agreement and bias between the two glucose measurements. Data from the external capsule, CC, CT and CPu were quantified for correlation analysis (six ROIs in total). Except for those processed by the aforementioned software, all other imaging data were processed via ImageJ (NIH, Bethesda, MD) and in house Matlab (Mathwork, Natick, MA) developed programs.

Statistical analysis.

Statistical analysis was performed by Welch's t-test with correction of unequal variances to examine the difference in image contrast between the normal and TBI brains using Prism v6.0c (GraphPad Software, Inc., La Jolla, CA). The significance level (α) was predetermined at 0.05 to reject the null hypothesis. The CoV was determined for the reproducibility of the glucoCEST data obtained from the ROIs in the 20 mM phantom and in CT for the brain. Pearson correlation and Bland-Altman analysis were performed to delineate the possible correlation and agreement/difference between the glucoCEST-weighted images and autoradiographs. Pearson correlation coefficient (r) and probability (p-value) were reported for the correlation analysis. Bias and 95% confidence interval (CI) were marked for the limits of agreement in the Bland-Altman plots. All data are reported as mean $\pm$ SD.

References

1. Ramlackhansingh, A. F. *et al.* Inflammation after trauma: microglial activation and traumatic brain injury. *Ann Neurol* **70**, 374–383 (2011).
2. Giza, C. C. & Hovda, D. A. The new neurometabolic cascade of concussion. *Neurosurgery* **75**, S24–33 (2014).
3. Johnson, V. E. *et al.* Inflammation and white matter degeneration persist for years after a single traumatic brain injury. *Brain* **136**, 28–42 (2013).
4. Peskind, E. R. *et al.* Cerebrocerebellar hypometabolism associated with repetitive blast exposure mild traumatic brain injury in 12 Iraq war Veterans with persistent post-concussive symptoms. *Neuroimage* **54**, S76–82 (2011).

5. Meierhans, R. *et al.* Brain metabolism is significantly impaired at blood glucose below 6 mM and brain glucose below 1 mM in patients with severe traumatic brain injury. *Crit Care* **14**, R13 (2010).
6. Giza, C. C. & Hovda, D. A. The Neurometabolic Cascade of Concussion. *J Athl Train* **36**, 228–235 (2001).
7. Selwyn, R. *et al.* Mild traumatic brain injury results in depressed cerebral glucose uptake: An (18)FDG PET study. *J Neurotrauma* **30**, 1943–1953 (2013).
8. Scafidi, S. *et al.* Delayed cerebral oxidative glucose metabolism after traumatic brain injury in young rats. *J Neurochem* **109**, 189–197 (2009).
9. Moro, N., Ghavim, S. S., Harris, N. G., Hovda, D. A. & Sutton, R. L. Pyruvate treatment attenuates cerebral metabolic depression and neuronal loss after experimental traumatic brain injury. *Brain Res* **1642**, 270–277 (2016).
10. Prins, M., Greco, T., Alexander, D. & Giza, C. C. The pathophysiology of traumatic brain injury at a glance. *Dis Model Mech* **6**, 1307–1315 (2013).
11. Kato, T. *et al.* Statistical image analysis of cerebral glucose metabolism in patients with cognitive impairment following diffuse traumatic brain injury. *J Neurotrauma* **24**, 919–926 (2007).
12. Gross, H., Kling, A., Henry, G., Herndon, C. & Lavretsky, H. Local cerebral glucose metabolism in patients with long-term behavioral and cognitive deficits following mild traumatic brain injury. *J Neuropsychiatry Clin Neurosci* **8**, 324–334 (1996).
13. Hattori, N. *et al.* Correlation of regional metabolic rates of glucose with glasgow coma scale after traumatic brain injury. *J Nucl Med* **44**, 1709–1716 (2003).
14. Wright, M. J. *et al.* Early metabolic crisis-related brain atrophy and cognition in traumatic brain injury. *Brain Imaging Behav* **7**, 307–315 (2013).
15. Baxter, L. R. Jr *et al.* Reduction of prefrontal cortex glucose metabolism common to three types of depression. *Arch Gen Psychiatry* **46**, 243–250 (1989).
16. Shively, S., Scher, A. I., Perl, D. P. & Diaz-Arrastia, R. Dementia resulting from traumatic brain injury: what is the pathology? *Arch Neurol* **69**, 1245–1251 (2012).
17. Sivanandam, T. M. & Thakur, M. K. Traumatic brain injury: a risk factor for Alzheimer's disease. *Neurosci Biobehav Rev* **36**, 1376–1381 (2012).
18. Messier, C. & Gagnon, M. Glucose regulation and cognitive functions: relation to Alzheimer's disease and diabetes. *Behav Brain Res* **75**, 1–11 (1996).
19. Vespa, P. *et al.* Metabolic crisis without brain ischemia is common after traumatic brain injury: a combined microdialysis and positron emission tomography study. *J Cereb Blood Flow Metab* **25**, 763–774 (2005).
20. Jalloh, I. *et al.* Glucose metabolism following human traumatic brain injury: methods of assessment and pathophysiological findings. *Metab Brain Dis* **30**, 615–632 (2015).
21. Byrnes, K. R. *et al.* FDG-PET imaging in mild traumatic brain injury: a critical review. *Front Neuroenergetics* **5**, 13 (2014).
22. Zhuang, H. *et al.* Dual time point 18F-FDG PET imaging for differentiating malignant from inflammatory processes. *J Nucl Med* **42**, 1412–1417 (2001).
23. Guivel-Scharen, V., Sinnwell, T., Wolff, S. D. & Balaban, R. S. Detection of proton chemical exchange between metabolites and water in biological tissues. *J Magn Reson* **133**, 36–45 (1998).
24. Ward, K. M., Aletras, A. H. & Balaban, R. S. A new class of contrast agents for MRI based on proton chemical exchange dependent saturation transfer (CEST). *J Magn Reson* **143**, 79–87 (2000).
25. Kogan, F., Hariharan, H. & Reddy, R. Chemical Exchange Saturation Transfer (CEST) Imaging: Description of Technique and Potential Clinical Applications. *Curr Radiol Rep* **1**, 102–114 (2013).
26. van Zijl, P. C. & Yadav, N. N. Chemical exchange saturation transfer (CEST): what is in a name and what isn't? *Magn Reson Med* **65**, 927–948 (2011).
27. Chan, K. W. *et al.* Natural D-glucose as a biodegradable MRI contrast agent for detecting cancer. *Magn Reson Med* **68**, 1764–1773 (2012).
28. Walker-Samuel, S. *et al. In vivo* imaging of glucose uptake and metabolism in tumors. *Nat Med* **19**, 1067–1072 (2013).
29. Xu, X. *et al.* Dynamic Glucose-Enhanced (DGE) MRI: Translation to Human Scanning and First Results in Glioma Patients. *Tomography* **1**, 105–114 (2015).
30. van Zijl, P. C., Jones, C. K., Ren, J., Malloy, C. R. & Sherry, A. D. MRI detection of glycogen *in vivo* by using chemical exchange saturation transfer imaging (glycoCEST). *Proc Natl Acad Sci USA* **104**, 4359–4364 (2007).
31. Tu, T. W. *et al.* Radiological-pathological correlation of diffusion tensor and magnetization transfer imaging in a closed head traumatic brain injury model. *Ann Neurol* **79**, 907–920 (2016).
32. Nasrallah, F. A., Pages, G., Kuchel, P. W., Golay, X. & Chuang, K. H. Imaging brain deoxyglucose uptake and metabolism by glucoCEST MRI. *J Cereb Blood Flow Metab* **33**, 1270–1278 (2013).
33. Chen, S. F. *et al.* Relationship between flow-metabolism uncoupling and evolving axonal injury after experimental traumatic brain injury. *J Cereb Blood Flow Metab* **24**, 1025–1036 (2004).
34. O'Connell, M. T. *et al.* Glucose metabolism in traumatic brain injury: a combined microdialysis and [18F]-2-fluoro-2-deoxy-D-glucose-positron emission tomography (FDG-PET) study. *Acta Neurochir Suppl* **95**, 165–168 (2005).
35. Rovlias, A. & Kotsou, S. The influence of hyperglycemia on neurological outcome in patients with severe head injury. *Neurosurgery* **46**, 335–342; discussion 342–333 (2000).
36. Rostami, E. Glucose and the injured brain-monitored in the neurointensive care unit. *Frontiers in neurology* **5**, 91 (2014).
37. Hillered, L., Persson, L., Nilsson, P., Ronne-Engstrom, E. & Enblad, P. Continuous monitoring of cerebral metabolism in traumatic brain injury: a focus on cerebral microdialysis. *Current opinion in critical care* **12**, 112–118 (2006).
38. Bellander, B. M. *et al.* Consensus meeting on microdialysis in neurointensive care. *Intensive care medicine* **30**, 2166–2169 (2004).
39. Reis, C. *et al.* What's New in Traumatic Brain Injury: Update on Tracking, Monitoring and Treatment. *International journal of molecular sciences* **16**, 11903–11965 (2015).
40. Haddad, S. H. & Arabi, Y. M. Critical care management of severe traumatic brain injury in adults. *Scandinavian journal of trauma, resuscitation and emergency medicine* **20**, 12 (2012).
41. Vespa, P. *et al.* Intensive insulin therapy reduces microdialysis glucose values without altering glucose utilization or improving the lactate/pyruvate ratio after traumatic brain injury. *Critical care medicine* **34**, 850–856 (2006).
42. Zafar, S. N., Iqbal, A., Farez, M. F., Kamatkar, S. & de Moya, M. A. Intensive insulin therapy in brain injury: a meta-analysis. *J Neurotrauma* **28**, 1307–1317 (2011).
43. Oddo, M. *et al.* Impact of tight glycemic control on cerebral glucose metabolism after severe brain injury: a microdialysis study. *Critical care medicine* **36**, 3233–3238 (2008).
44. Bergsneider, M. *et al.* Dissociation of cerebral glucose metabolism and level of consciousness during the period of metabolic depression following human traumatic brain injury. *J Neurotrauma* **17**, 389–401 (2000).
45. Lin, A. P. *et al.* Metabolic imaging of mild traumatic brain injury. *Brain Imaging Behav* **6**, 208–223 (2012).
46. Golding, E. M., Robertson, C. S. & Bryan, R. M. Jr. The consequences of traumatic brain injury on cerebral blood flow and autoregulation: a review. *Clin Exp Hypertens* **21**, 299–332 (1999).
47. Balabanov, R. *et al.* Endothelial cell activation following moderate traumatic brain injury. *Neurol Res* **23**, 175–182 (2001).
48. Shiga, T. *et al.* Loss of neuronal integrity: a cause of hypometabolism in patients with traumatic brain injury without MRI abnormality in the chronic stage. *European journal of nuclear medicine and molecular imaging* **33**, 817–822 (2006).
49. Bartnik, B. L. *et al.* Upregulation of pentose phosphate pathway and preservation of tricarboxylic acid cycle flux after experimental brain injury. *J Neurotrauma* **22**, 1052–1065 (2005).

50. Wang, J. *et al*. Magnetic Resonance Imaging of Glucose Uptake and Metabolism in Patients with Head and Neck Cancer. *Sci Rep* **6**, 30618 (2016).

51. Wang, F. *et al*. Mapping murine diabetic kidney disease using chemical exchange saturation transfer MRI. *Magn Reson Med* **76**, 1531–1541 (2015).

52. Dula, A. N. *et al*. Development of chemical exchange saturation transfer at 7 T. *Magn Reson Med* **66**, 831–838 (2011).

53. Dula, A. N., Smith, S. A. & Gore, J. C. Application of chemical exchange saturation transfer (CEST) MRI for endogenous contrast at 7 Tesla. *J Neuroimaging* **23**, 526–532 (2013).

54. Haris, M., Cai, K., Singh, A., Hariharan, H. & Reddy, R. *In vivo* mapping of brain myo-inositol. *Neuroimage* **54**, 2079–2085 (2011).

55. Bonvento, G., Valette, J., Flament, J., Mochel, F. & Brouillet, E. Imaging and spectroscopic approaches to probe brain energy metabolism dysregulation in neurodegenerative diseases. *J Cereb Blood Flow Metab* **37**, 1927–1943 (2017).

56. Dula, A. N. *et al*. Optimization of 7-T chemical exchange saturation transfer parameters for validation of glycosaminoglycan and amide proton transfer of fibroglandular breast tissue. *Radiology* **275**, 255–261 (2015).

57. Kim, J., Wu, Y., Guo, Y., Zheng, H. & Sun, P. Z. A review of optimization and quantification techniques for chemical exchange saturation transfer MRI toward sensitive *in vivo* imaging. *Contrast Media Mol Imaging* **10**, 163–178 (2015).

58. Sun, P. Z., van Zijl, P. C. & Zhou, J. Optimization of the irradiation power in chemical exchange dependent saturation transfer experiments. *J Magn Reson* **175**, 193–200 (2005).

59. Heo, H. Y. *et al*. Whole-brain amide proton transfer (APT) and nuclear overhauser enhancement (NOE) imaging in glioma patients using low-power steady-state pulsed chemical exchange saturation transfer (CEST) imaging at 7T. *J Magn Reson Imaging* **44**, 41–50 (2016).

60. Schwartz, W. J. & Sharp, F. R. Autoradiographic maps of regional brain glucose consumption in resting, awake rats using (14C) 2-deoxyglucose. *J Comp Neurol* **177**, 335–359 (1978).

61. Duncan, G. E., Miyamoto, S., Leipzig, J. N. & Lieberman, J. A. Comparison of brain metabolic activity patterns induced by ketamine, MK-801 and amphetamine in rats: support for NMDA receptor involvement in responses to subanesthetic dose of ketamine. *Brain Res* **843**, 171–183 (1999).

62. Vissing, J., Andersen, M. & Diemer, N. H. Exercise-induced changes in local cerebral glucose utilization in the rat. *J Cereb Blood Flow Metab* **16**, 729–736 (1996).

63. Ashwal, S. *et al*. Proton spectroscopy detected myoinositol in children with traumatic brain injury. *Pediatr Res* **56**, 630–638 (2004).

64. Babikian, T. *et al*. MR spectroscopy: predicting long-term neuropsychological outcome following pediatric TBI. *J Magn Reson Imaging* **24**, 801–811 (2006).

65. Pascual, J. M. *et al*. Time course of early metabolic changes following diffuse traumatic brain injury in rats as detected by (1)H NMR spectroscopy. *J Neurotrauma* **24**, 944–959 (2007).

66. Budde, M. D., Janes, L., Gold, E., Turtzo, L. C. & Frank, J. A. The contribution of gliosis to diffusion tensor anisotropy and tractography following traumatic brain injury: validation in the rat using Fourier analysis of stained tissue sections. *Brain* **134**, 2248–2260 (2011).

67. Prieto, E. *et al*. Statistical parametric maps of (1)(8)F-FDG PET and 3-D autoradiography in the rat brain: a cross-validation study. *European journal of nuclear medicine and molecular imaging* **38**, 2228–2237 (2011).

68. Heo, H. Y. *et al*. Insight into the quantitative metrics of chemical exchange saturation transfer (CEST) imaging. *Magn Reson Med* **77**, 1853–1865 (2017).

69. Heo, H. Y., Zhang, Y., Jiang, S., Lee, D. H. & Zhou, J. Quantitative assessment of amide proton transfer (APT) and nuclear overhauser enhancement (NOE) imaging with extrapolated semisolid magnetization transfer reference (EMR) signals: II. Comparison of three EMR models and application to human brain glioma at 3 Tesla. *Magn Reson Med* **75**, 1630–1639 (2016).

70. Desmond, K. L., Moosvi, F. & Stanisz, G. J. Mapping of amide, amine, and aliphatic peaks in the CEST spectra of murine xenografts at 7 T. *Magn Reson Med* **71**, 1841–1853 (2014).

71. Zaiss, M., Schmitt, B. & Bachert, P. Quantitative separation of CEST effect from magnetization transfer and spillover effects by Lorentzian-line-fit analysis of z-spectra. *J Magn Reson* **211**, 149–155 (2011).

72. Jin, T., Mehrens, H., Hendrich, K. S. & Kim, S. G. Mapping brain glucose uptake with chemical exchange-sensitive spin-lock magnetic resonance imaging. *J Cereb Blood Flow Metab* **34**, 1402–1410 (2014).

73. Zu, Z., Spear, J., Li, H., Xu, J. & Gore, J. C. Measurement of regional cerebral glucose uptake by magnetic resonance spin-lock imaging. *Magnetic resonance imaging* **32**, 1078–1084 (2014).

74. Singh, A., Cai, K., Haris, M., Hariharan, H. & Reddy, R. On B1 inhomogeneity correction of *in vivo* human brain glutamate chemical exchange saturation transfer contrast at 7T. *Magn Reson Med* **69**, 818–824 (2013).

75. Klomp, D. W. *et al*. Amide proton transfer imaging of the human breast at 7T: development and reproducibility. *NMR in biomedicine* **26**, 1271–1277 (2013).

76. Dula, A. N. *et al*. Amide proton transfer imaging of the breast at 3T: establishing reproducibility and possible feasibility assessing chemotherapy response. *Magn Reson Med* **70**, 216–224 (2013).

77. Liu, G., Song, X., Chan, K. W. & McMahon, M. T. Nuts and bolts of chemical exchange saturation transfer MRI. *NMR in biomedicine* **26**, 810–828 (2013).

78. Silver, I. A. & Erecinska, M. Extracellular glucose concentration in mammalian brain: continuous monitoring of changes during increased neuronal activity and upon limitation in oxygen supply in normo-, hypo-, and hyperglycemic animals. *J Neurosci* **14**, 5068–5076 (1994).

79. Cai, K. *et al*. Magnetic resonance imaging of glutamate. *Nat Med* **18**, 302–306 (2012).

80. Kim, M., Gillen, J., Landman, B. A., Zhou, J. & van Zijl, P. C. Water saturation shift referencing (WASSR) for chemical exchange saturation transfer (CEST) experiments. *Magn Reson Med* **61**, 1441–1450 (2009).

81. National Research Council (U.S.). Committee for the Update of the Guide for the Care and Use of Laboratory Animals., Institute for Laboratory Animal Research (U.S.) & National Academies Press (U.S.). *Guide for the care and use of laboratory animals*. 8th edn, (National Academies Press, 2011).

82. Tu, T. W. *et al*. Imaging of spontaneous ventriculomegaly and vascular malformations in Wistar rats: implications for preclinical research. *Journal of neuropathology and experimental neurology* **73**, 1152–1165 (2014).

83. Sun, P. Z., Lu, J., Wu, Y., Xiao, G. & Wu, R. Evaluation of the dependence of CEST-EPI measurement on repetition time, RF irradiation duty cycle and imaging flip angle for enhanced pH sensitivity. *Phys Med Biol* **58**, N229–240 (2013).

Acknowledgements

Author Contributions

T.W.T., J.M., D.H. and J.A.F. designed the experiments. T.W.T., W.I., N.J. and J.W. carried out the experiments and analyzed the data. T.W.T., J.M. and J.A.F. wrote the paper. All authors reviewed the manuscript.

Additional Information